Homogenisation method for braced excavations stabilised with deep-mixed columns

Computers and Geotechnics 181 (2025) 107095

Contents lists available at ScienceDirect

Computers and Geotechnics

journal homepage: www.elsevier.com/locate/compgeo

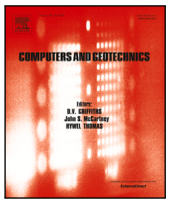

Research paper

Homogenisation method for braced excavations stabilised with deep-mixed columns

Sinem Bozkurt *, Ayman Abed, Minna Karstunen

Chalmers University of Technology, Department of Architecture and Civil Engineering, Gothenburg, SE-412 96, Sweden

ARTICLE INFO

Keywords:
Deep excavation
Volume averaging
Deep mixing
Lime-cement columns
Soft clay

ABSTRACT

The stabilisation of deep excavations using columnar inclusions introduces three-dimensional (3D) complexities into design calculations. Often the intricate nature of the wall-soil-column interaction is simulated using simplified averaging techniques based on elasticity theory. This paper introduces a numerical technique to accurately describe the nonlinear elastoplastic response of both stabilised and natural soft clay for the case of excavations stabilised with deep-mixed columns. The technique allows mapping the 3D problem into a plane-strain (2D) counterpart by replacing the composite material made of natural clay and a region of overlapping deep-mixed columns with an equivalent homogenised material. The stress–strain response of the homogenised continuum is computed with a volume averaging technique (VAT) based on the volume fraction of each component (i.e. clay and column). The technique is implemented into a 2D finite element code enabling an effective representation of the behaviour of each constituent represented by advanced elastoplastic material models. After presenting the theoretical background and implementation procedure, the proposed method was verified against the results from the 3D calculations. The technique emerges as an efficient tool for the numerical analysis of stabilised deep excavations since it allows for plane strain analysis to yield results akin to computationally expensive 3D analysis. Thus, the method can significantly reduce the computational costs and can facilitate the easier incorporation of sensitivity studies.

1. Introduction

Ground improvement techniques using columnar inclusions (e.g. stone columns and lime-cement (LC) columns) are widely employed in soft clays to reduce settlements and increase the stability due to their ability to enhance the soil properties *in situ*. In the numerical analysis, to account for the three dimensional (3D) nature of the stabilised clay with the inclusions, and the complexity of column and soil interaction, the stabilised region can be represented by a composite material consisting of two components. When simplifying the macroscopic heterogeneous structure, the composite material can be regarded as an anisotropic homogeneous continuum (Hill, 1963; Hashin, 1983; Canetta and Nova, 1989; Anglade et al., 2023). The homogenised soil can then be modelled with an equivalent material by averaging the constitutive behaviour of the surrounding soil and columns based on their volume fractions (i.e. the volume occupied by each constituent). The resulting equivalent material represents a stabilised soil in which the inclusions are uniformly and homogeneously distributed. The homogenisation procedure can be formulated employing different constitutive soil models for the *in situ* soil and the inclusions provided that local equilibrium and kinematics within the homogenised medium are satisfied for both elastic and elasto- or visco-plastic conditions.

The homogenisation technique has been primarily utilised for the analysis of fractures in porous media (e.g. Dvorak and Zhang, 2001; Levasseur et al., 2011; Bharali et al., 2021) and for the analysis of laminated structures with fibres (e.g. Dvorak and Bahei-El-Din, 1979; Hashin, 1983; Idesman et al., 1996; van der Sluis et al., 1999). In the geotechnical field, the technique has been employed in numerical analyses, with a particular focus on the foundation of embankments (i.e. Schweiger and Pande, 1988; Canetta and Nova, 1989; Lee and Pande, 1998; Omine et al., 1998; Jellali et al., 2005; Vogler, 2009; Omine et al., 2017). These numerical analyses aimed to find a way to improve the stability of soil beneath railway and highway structures while taking into account the volume fractions of the inclusions.

The success of the homogenisation technique in accurately reflecting the stabilised soil response relies heavily on fulfilling the local mechanical balance conditions and maintaining the continuity of the kinematics of the strain field at the interface between the columnar inclusions and *in situ* soil. Notably, the stress–strain response of the stabilised clay in deep excavations is significantly influenced by 3D effects which may not be adequately captured by a two-dimensional

* Corresponding author.
E-mail address: sinem.bozkurt@chalmers.se (S. Bozkurt).

https://doi.org/10.1016/j.compgeo.2025.107095
Received 4 November 2024; Received in revised form 20 December 2024; Accepted 15 January 2025
Available online 5 February 2025

(2D) numerical analysis (Zdravkovic et al., 2005; Finno et al., 2007). Although 3D simulations offer a more accurate representation of field response, they are more time-consuming, computationally expensive, and less readily available than 2D analysis tools.

Applying homogenisation technique to stabilised deep excavations has not been investigated yet, as first, the equilibrium and continuity constraints of the equivalent continuum need to be identified. Therefore, in this study, the distinct nonlinear stress–strain responses of the constituents of the LC columns and soft clay are investigated by performing a fully coupled 3D consolidation calculation. Based on this analysis, the local equilibrium and kinematic constraints are identified and used to develop a volume averaging technique (VAT) for a corresponding 2D analysis. The adopted VAT follows a similar methodology described in Lee and Pande (1998), Vogler and Karstunen (2008) and Vogler (2009) but account for the different boundary conditions. The technique allows for the use of different advanced soil models representing the clay and column materials, respectively, providing computational efficiency while capturing results that are comparable to those of 3D simulations.

Our main contribution lies in the analytical establishment of the equilibrium and continuity constraints within soft clay and deep-mixed columns for a case of braced excavation, and in successfully applying the developed theory to a boundary value problem in plane strain conditions. Specifically, the method is implemented in a way that restores equilibrium as well as maintains the continuity of kinematics while using different advanced constitutive models. Consequently, the technique eliminates the need for 3D models and the associated computational costs, making it particularly advantageous for modelling a large number of columns arranged in a periodic grid.

2. Computational framework of the volume averaging technique for deep excavations

To calculate the overall response of a deep excavation stabilised with deep-mixed columns using a homogenisation technique, the stresses and strains within the stabilised region were assumed to be distributed across the columns and soft clay, based on their respective volume fractions. The technique involves computing the equivalent stress and strain increments ($\Delta\sigma^{eq}$ and $\Delta\varepsilon^{eq}$) in the equivalent homogenised material using the volume fraction of the soft clay and columns, denoted as Ω_s and Ω_c, respectively. The computation is given by Eqs. (1)–(3) :

$$\Delta\sigma^{eq} = \Omega_s \Delta\sigma^{s} + \Omega_c \Delta\sigma^{c} \tag{1}$$

$$\Delta\varepsilon^{eq} = \Omega_s \Delta\varepsilon^{s} + \Omega_c \Delta\varepsilon^{c} \tag{2}$$

$$\Delta\sigma^{eq} = D^{eq} \Delta\varepsilon^{eq} \tag{3}$$

Here, D^{eq} denotes the stiffness matrix of the equivalent material, which is a function of volume fraction and the stiffness matrices of the constituents. The volume fractions of Ω_c and Ω_s can be defined for evenly distributed columns without overlapping using Eqs. (4) and (5), respectively.

$$\Omega_c = \pi \frac{r_c^2}{s_c^2} \tag{4}$$

$$\Omega_s = 1 - \Omega_c \tag{5}$$

where the column radius is r_c and the column spacing is s_c. Alternatively, in the case of overlapping columns, the column area can be calculated by simplifying the geometry into a rectangular form, as demonstrated in Fig. 1. Through the application of averaging rules, while simultaneously satisfying the predefined local equilibrium and kinematic conditions, it becomes possible to determine the equivalent stiffness matrix through analytical means. In this study, the prescribed local equilibrium and kinematic conditions are established based on a 3D simulation of an excavation.

Table 1
Construction stages used in the FE analysis.

Phase number	Phase	Time interval [days]
0	Initial state	–
1	Installation of SPW	20
2	LC column installation	30
3	Excavation to −2 level	10
4	Excavation to −5 level	10

The following Sections 2.1 and 2.2, describe the 3D benchmark model and the constitutive models utilised in the numerical simulations. The 3D benchmark simulation consists of a numerical analysis of a stabilised braced excavation taking into account transient flow for an arbitrary consolidation period. The parameters for the constitutive models were calculated and calibrated based on extensive laboratory testing data for both the stabilised clay, using the dry soil mixing method (DSM), and the natural clay. The laboratory test data relate to an excavation site in Gothenburg, Sweden (Bozkurt et al., 2023). The calibrated parameters were used to simulate a simplified excavation problem to represent soil behaviour under field conditions.

2.1. Numerical model of a deep excavation

The numerical analysis involved the simulation of a 5 m deep braced excavation stabilised with LC columns. The benchmark analysis employed a 3D model combined with a fully coupled consolidation analysis. Finite element analysis (FEA) was performed using PLAXIS 3D (version 23). The braced excavation was assumed to be supported by a 15 m long sheet pile wall (SPW), complemented by a single row of struts spaced at 5 m intervals. The deep-mixed columns were installed along the first 10 m of the passive side of the excavation.

The construction sequence is detailed in Table 1. Preceding the installation of LC columns, SPW was put in place. Subsequently, along the passive side of the excavation, LC columns were constructed. The columns were formed using double overlapping DSM columns, each with a diameter of 70 cm, arranged in a square grid pattern with a spacing of 2.5 m and a 20 cm overlap. Struts were installed at level −0.8 as the soil was excavated to level −2.

In the 3D FEA, the grid of LC columns was simplified to a rectangular form, and columns and soft clay were simulated using different clusters of material, as demonstrated in Fig. 1. First, a special investigation into mesh dependency was performed, focusing on mesh refinement around the excavation area where high-stress gradients are expected due to the presence of structural elements, such as LC columns, struts and SPW. The study resulted in a final mesh that consists of 42,294 ten-noded tetrahedral elements with each element incorporating 4 Gaussian integration points and 67,835 nodes for the 3D model. The finalised excavation geometry is presented in Fig. 1. Standard fixities were applied as displacement boundary conditions. The hydraulic boundary at the bottom was modelled as impermeable. Additionally, SPW was assumed to be impermeable, preventing any seepage through the wall.

In the subsequent numerical analyses, to simulate the stress–strain response of the soft clay and the deep-mixed columns, the S-CLAY1S (Koskinen et al., 2002; Karstunen et al., 2005) and MNhard (Benz et al., 2008) constitutive models were utilised, introduced in the following section.

- **S-CLAY1S model for soft clay**

The S-CLAY1S model (Koskinen et al., 2002; Karstunen et al., 2005) is a critical state model that was developed to describe the behaviour of normally consolidated and lightly overconsolidated natural clays in the wet side of the critical state line. The model is an extension of the S-CLAY1 model (Wheeler et al., 2003), to account for the destructuration resulting from the degradation of interparticle bonding. The model incorporates the influence of the initial (inherent) anisotropy and the

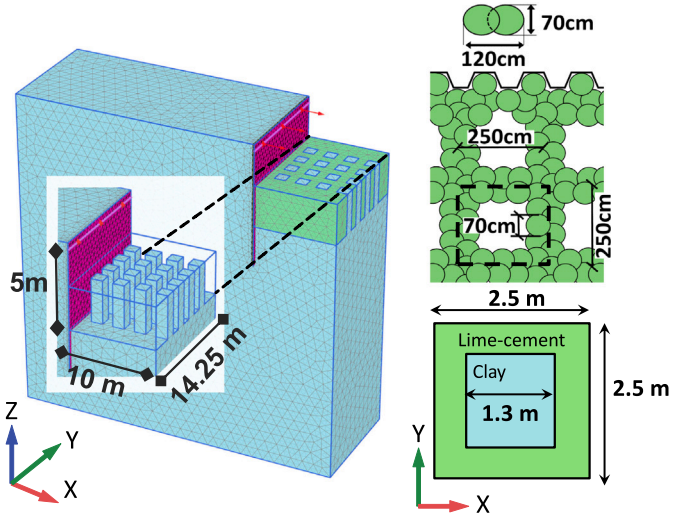

Fig. 1. 3D numerical model of the deep excavation.

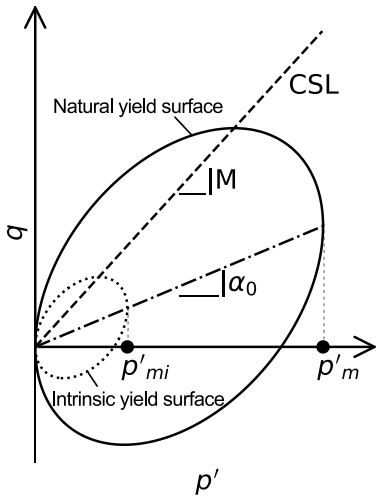

Fig. 2. Yield surface of S-CLAY1S model in triaxial stress space.

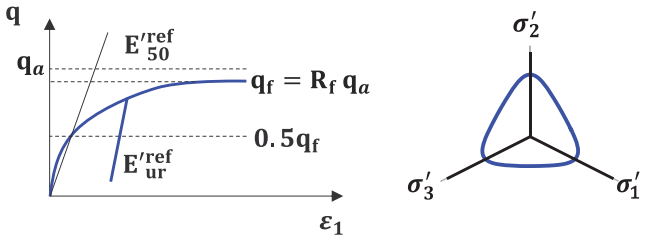

Fig. 3. MNhard soil model in triaxial stress states.

evolution of anisotropy defined by an inclined yield surface. The effects of bonding and destructuration are modelled by using the concept of intrinsic yield surface (Gens and Nova, 1993). The intrinsic yield surface describes the imaginary yield surface of the same soil with the same void ratio at a state where all bonding is removed. The S-CLAY1S model formulation does not include strain rate effects which were later on incorporated into the formulation of the Creep-S-CLAY1S model by Sivasithamparam et al. (2013, 2015) and Gras et al. (2018) to enable simulating the strain rate-dependency of natural clay response.

In this research, the lightly overconsolidated soft clay was represented by the S-CLAY1S model. In triaxial stress states, the yield surface of the S-CLAY1S model is expressed by Eq. (6) and is illustrated in Fig. 2.

$$f = (q - \alpha p')^2 - (M^2 - \alpha^2)(p'_m - p')p' = 0 \tag{6}$$

where $q = (\sigma'_1 - \sigma'_3)$ is the deviatoric stress and the mean effective stress $p' = (\sigma'_1 + 2\sigma'_3)/3$, M is the stress ratio at the critical state and α defines the orientation of the surface. The initial isotropic preconsolidation pressure, p'_m can be related to the size of the intrinsic yield surface, p'_{mi} through the amount of bonding, χ (in Eq. (7)).

$$p'_m = (1 + \chi)p'_{mi} \tag{7}$$

The three hardening laws used in the model define the changes in the size of the intrinsic yield surface, the progressive loss of bonding and the rotation of the yield surface due to plastic straining. The generalised formulation of the model in 3D stress space is presented in Appendix A.

The values for the model parameters were selected following a prior study by Bozkurt et al. (2023), using several CAUE/CADE (anisotropically consolidated undrained/drained triaxial tests in extension) and IL (incrementally loaded oedometer) tests performed on natural clay samples. The calibration of the model parameters was conducted through numerical simulations of the laboratory tests (see Appendix C) focussing on extension side, aiming to ensure the application of realistic parameters for the numerical analysis of a stabilised excavation in soft natural clay. The parameters employed in the simulations are given in Table 2.

The vertical and horizontal hydraulic conductivities along the soil profile are assumed to be of the same order ($k_v = k_h$), approximately 0.75×10^{-4} m/day, along with a permeability change index, c_k of 0.27 ($c_k = (e_0 - e)/\log(k_0/k)$, where k_0 denotes the hydraulic conductivity corresponding to e_0 and k is the current hydraulic conductivity at the current void ratio, e).

• MNhard model for LC columns

The Matsuoka–Nakai Hardening material model (MNhard) (Benz et al., 2008) has a comparable formulation with the widely known Hardening Soil model (HS) (Schanz, 1998; Schanz et al., 1999). However, unlike HS, the MNhard model does not account for volumetric hardening and employs the Matsuoka–Nakai (MN) failure criterion (Matsuoka and Nakai, 1974; Matsuoka, 1976), instead of the Mohr–Coulomb criterion. The MN failure criterion uses the concept of the average of mobilised planes (SPM, 'spatially mobilised plane') in three-dimensional stress space (Matsuoka and Nakai, 1982, 1985). The validity of the MN failure criterion has been evidenced through its success in accurately predicting soil failure, where intermediate stress differs from both minor and major stresses, in element tests, as well as in boundary value problems (Nakai and Matsuoka, 1983). The shear hardening during triaxial primary loading is described by the yield function in Eq. (8) (see Fig. 3).

$$f_s = \frac{3}{4}\frac{q_a}{E'_{50}}\frac{q}{q_a - q} - \frac{3}{2}\frac{2q}{E'_{ur}} - \gamma_s^{ps} \;\; and \;\; R_f = \frac{q_f}{q_a} < 1.0 \tag{8}$$

where E'_{50} and E'_{ur} represent the secant and unloading-reloading stiffnesses, while γ_s^{ps} describes the accumulated deviatoric plastic shear strain ($\gamma_s^{ps} = 3/2\epsilon_1^p$) (Benz et al., 2008). The yield locus expands with plastic shear strains resulting from deviatoric loading until the MN failure surface is reached. q_a is the asymptotic deviatoric stress, as defined in the original hypoplastic Duncan–Chang model, which was later extended to the elastoplastic HS model by Schanz (1998). q_f is the deviatoric stress at failure and R_f is the failure ratio. A brief description of the model is presented in Appendix B.

The model incorporates an effective minor stress-dependent stiffness as per Eq. (9).

$$E'_{50} = E'^{\,ref}_{50}\left(\frac{\sigma'_3 + c'\cot\phi'}{\sigma'^{ref} + c'\cot\phi'}\right)^m \tag{9}$$

Table 2
S-CLAY1S model parameters for soft clay.

Type	Definition	Value [–]
Stiffness	κ, slope of the swelling line	0.02
	λ_i, slope of the intrinsic normal compression line	0.2
	ν', Poisson's ratio	0.2
Strength	M, stress ratio at critical state	1.10
Anisotropy	μ, absolute effectiveness of rotational hardening	50
	β, relative effectiveness of rotational hardening	0.64
Destructuration	a, absolute rate of destructuration due to volumetric strain	12
	b, relative rate of destructuration due to shear strain	0.4
Initialisation	e_0, initial void ratio	1.90
	α_0, initial anisotropy	0.42
	χ_0, initial amount of bonding	6
	OCR, overconsolidation ratio (–)	1.20
	K_0, coefficient of earth pressure at rest	0.54

Table 3
MNhard soil parameters for lime-cement columns.

γ_n (kN/m^3)	G_{50}^{ref} (kPa)	G_{ur}^{ref} (kPa)	p^{ref} (kPa)	m	ϕ' (°)	c' (kPa)	ν'
17	28 000	75 000	100	0.65	37	20	0.25

where $E'_{50}{}^{ref}$ is a reference secant modulus corresponding to a reference stress σ'^{ref}, σ'_3 is the minor effective stress, and the exponent of m is a model parameter that reflects the stress-dependency of the stiffness of the material.

The unloading and reloading is assumed to be purely elastic. The secant unloading-reloading modulus is analogously expressed by Eq. (10). The shear modulus can be defined by elasticity theory with the effective Poisson's ratio, ν' and E'_{ur}.

$$E'_{ur} = E'_{ur}{}^{ref}\left(\frac{\sigma'_3 + c'\cot\phi'}{\sigma'^{ref} + c'\cot\phi'}\right)^m \tag{10}$$

The values for the model parameters of the LC columns, detailed in Table 3, were derived based on CAUE tests performed on both laboratory-mixed and field-mixed samples, as outlined in Bozkurt et al. (2023). The calibration of the MNhard model parameters, using undrained triaxial test results, was with the SoilTest facility in the PLAXIS 2D FE code. The permeability of the LC columns was computed from IL tests, and the values were close to those of the natural clay as presented in Section 2.1. This study adopts the same soil model parameters for the LC columns using the MNhard model as in Bozkurt et al. (2023).

2.2. Stress–strain response of LC columns and natural clay

The distinct responses of the soft natural clay and the LC columns within the stabilised region were examined separately by analysing stress–strain distribution in the clay/column system using a 3D model. The global coordinate system is set up with x and y as the horizontal directions and z as the vertical direction. Throughout the paper, the geotechnical engineering sign convention is used. Compressive stresses and contractive strains are denoted by a positive sign, while a negative sign corresponds to tensile stresses and expansive strains.

The responses of the clay and columns were described by different constitutive models employing the S-CLAY1S and MNhard models, respectively. The high rigidity of the column compared to the natural clay, and the use of different constitutive soil models resulted in different stress paths within each material. In the 3D analysis, the stress–strain response of the constituents was investigated at representative locations projected onto the plan view shown in Fig. 4, in the final excavation phase over a 70-day consolidation period (see Table 1). The sampling points are taken from the midsection, and the stress–strain responses of the clay and stabilising materials are plotted at the final excavation stage along the stabilised region (depths −5 to −10) in Fig. 5.

Based on the results of the simulation, the stress and strain increments within the clay and columns are analogous in some directions as illustrated in Figs. 5(a)–5(f). Thus, based on the 3D FEA, the stress–strain equality conditions between each constituent were generalised to evaluate the response of the equivalent material. The horizontal stress increment ($\Delta\sigma_{yy}$) perpendicular to the plane direction and shear stress increments ($\Delta\tau_{xy}$ and $\Delta\tau_{yz}$) were found to be comparable between the clay and columns as illustrated in Fig. 6. The stress equality in the clay/column system leads to a uniform stress distribution following Reuss assumptions (Reuss, 1929) in stated directions in Eqs. (11)–(13).

$$\Delta\sigma^{eq}_{yy} = \Delta\sigma^{c}_{yy} = \Delta\sigma^{s}_{yy} \tag{11}$$

$$\Delta\tau^{eq}_{xy} = \Delta\tau^{c}_{xy} = \Delta\tau^{s}_{xy} \tag{12}$$

$$\Delta\tau^{eq}_{yz} = \Delta\tau^{c}_{yz} = \Delta\tau^{s}_{yz} \tag{13}$$

Similarly, analogous kinematic conditions were projected for the increments of vertical strains ($\Delta\varepsilon_{zz}$), horizontal strains ($\Delta\varepsilon_{xx}$) and shear strains ($\Delta\gamma_{zx}$) in both the column and clay materials considering perfect bonding (in Fig. 7). The generalised equal strain increments within the homogenised clay calculated using the 3D simulation align with Voigt (Voigt, 1889) assumptions in specific directions as given in Eqs. (14)–(16).

$$\Delta\varepsilon^{eq}_{xx} = \Delta\varepsilon^{c}_{xx} = \Delta\varepsilon^{s}_{xx} \tag{14}$$

$$\Delta\varepsilon^{eq}_{zz} = \Delta\varepsilon^{c}_{zz} = \Delta\varepsilon^{s}_{zz} \tag{15}$$

$$\Delta\gamma^{eq}_{zx} = \Delta\gamma^{c}_{zx} = \Delta\gamma^{s}_{zx} \tag{16}$$

Additionally, for the same cross-sections, the horizontal and vertical deformation distributions in the clay and the LC columns within the improved zone were compared, as shown in Fig. 8. The sampling points along the z-axis at depths between −5 and −10 were investigated (see Fig. 4).

The local equilibrium and compatibility conditions of the homogenised medium consisting of deep-mixed columns and *in situ* natural clay were thus derived through the 3D analysis. The fundamental assumptions that form the basis of the homogenisation method for an excavation case based on the analysis are proposed as:

- Columns are homogeneously and uniformly distributed over the reinforced region in the passive side of the excavation
- The vertical strains, horizontal strains (in the horizontal plane direction) and shear strains (angular strain in the vertical plane) in both the column and *in situ* clay are equal, so no slippage is allowed
- The continuity of the horizontal stress (in the out-of-plane direction) and of the shear stresses (in vertical and horizontal directions) between the clay and the columns are ensured

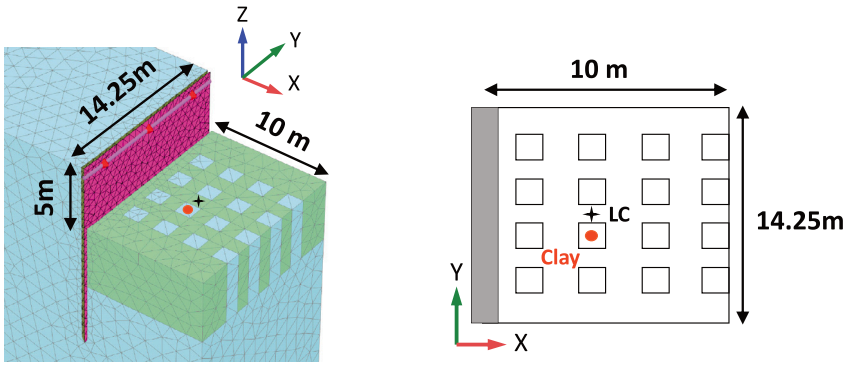

Fig. 4. Sampling locations in the 3D FEA: (a) 3D view; (b) plan view.

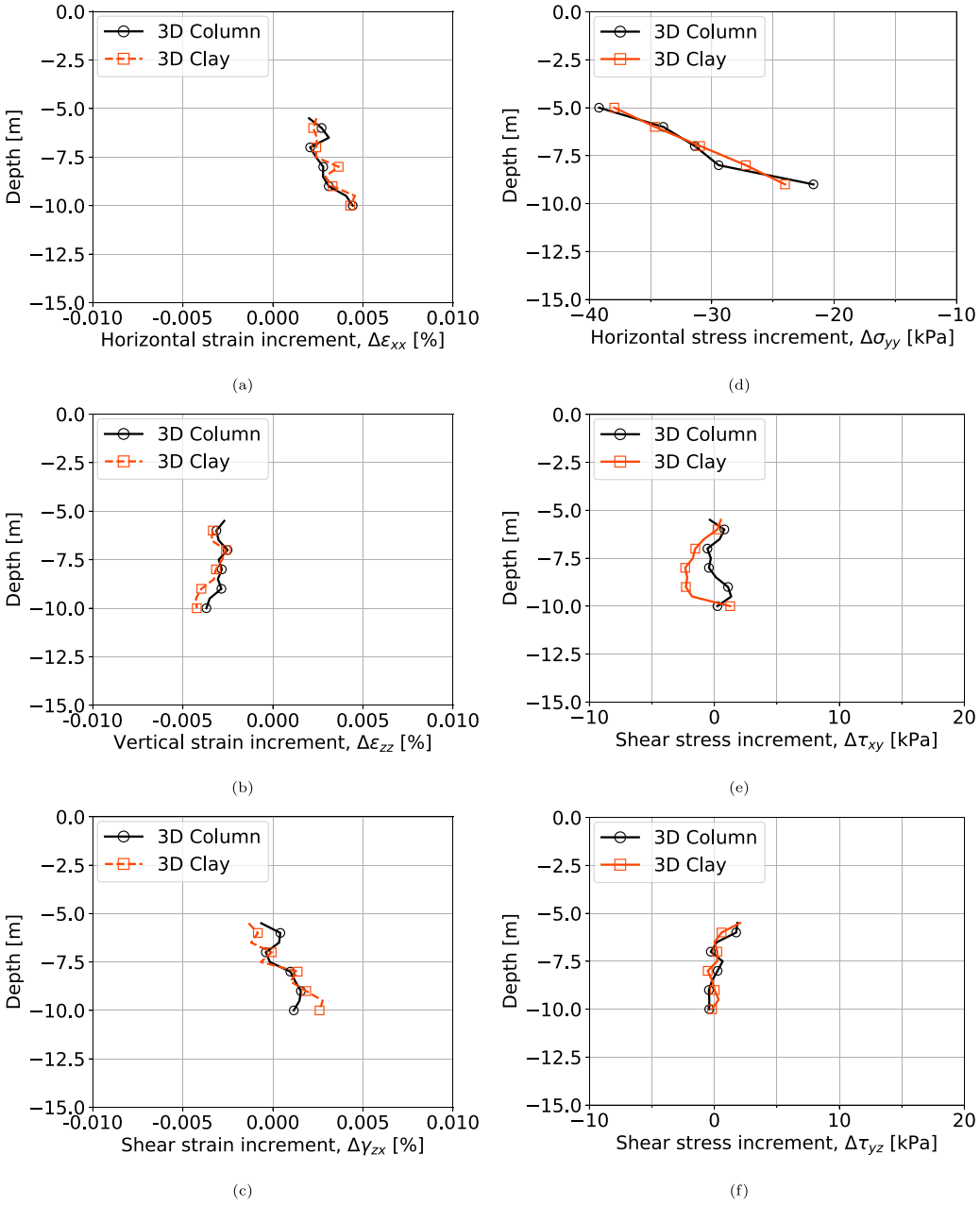

Fig. 5. Stress–strain increments in the clay/column system at the final excavation stage in the 3D FEA.

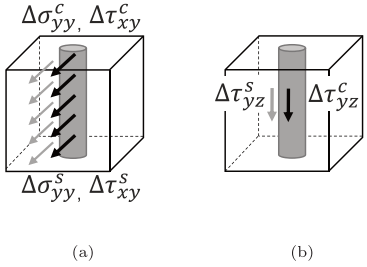

Fig. 6. Generalised equal stress increments in clay/column system: (a) horizontal stress increment, $\Delta\sigma_{yy}$ and shear stress increment, $\Delta\tau_{xy}$; (b) shear stress increment, $\Delta\tau_{yz}$.

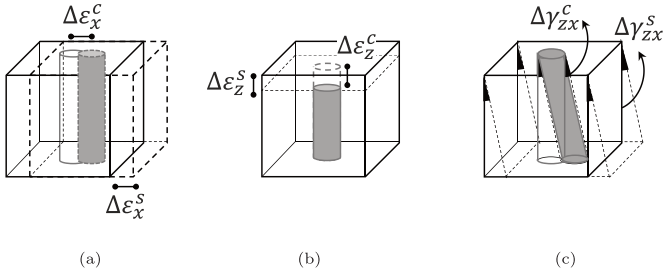

Fig. 7. Generalised equal strain increments in clay/column system: (a) horizontal strain, $\Delta\varepsilon_{xx}$; (b) vertical strain, $\Delta\varepsilon_{zz}$; (c) shear strain, $\Delta\gamma_{zx}$.

- The columns are placed vertically

3. Constitutive modelling of the equivalent continuum

The construction of the elastic constitutive matrix of the equivalent material, $\mathbf{D^{eq}}$ describing the behaviour of the stabilised clay system requires the full *6*6* elastic stiffness matrix, **D** of the column and the natural clay. Since the formulation of the S-CLAY1S model, implemented in PLAXIS 2D by Wiltafsky (2003) (and all soil models in PLAXIS are done with 3D in mind), the integration of the system of nonlinear equations includes all tensorial components. $\mathbf{D^{eq}}$ can be calculated using Eq. (17), for a plane strain analysis. The global coordinate system in a 2D analysis in PLAXIS defines x and z as the horizontal directions, while y indicates the vertical direction (Hence, when employing established relationships for VAT in 3D analysis with PLAXIS, it becomes necessary to invert the definitions of the y and z axes).

$$\begin{bmatrix}\sigma_x\\ \sigma_y\\ \sigma_z\\ \tau_{xy}\\ \tau_{yz}\\ \tau_{zx}\end{bmatrix}_{eq} = \begin{bmatrix}D_{11} & D_{12} & D_{13} & D_{14} & D_{15} & D_{16}\\ D_{21} & D_{22} & D_{23} & D_{24} & D_{25} & D_{26}\\ D_{31} & D_{32} & D_{33} & D_{34} & D_{35} & D_{36}\\ D_{41} & D_{42} & D_{43} & D_{44} & D_{36} & D_{46}\\ D_{51} & D_{52} & D_{53} & D_{45} & D_{37} & D_{56}\\ D_{61} & D_{62} & D_{63} & D_{46} & D_{38} & D_{66}\end{bmatrix}_{eq} \begin{bmatrix}\varepsilon_x\\ \varepsilon_y\\ \varepsilon_z\\ \gamma_{xy}\\ \gamma_{yz}\\ \gamma_{zx}\end{bmatrix}_{eq} \tag{17}$$

$\mathbf{D^{eq}}$ can be determined analytically by using the volume fraction of each constituent and the predefined kinematic and continuity conditions obtained from the full 3D analysis. The volume fractions of the column and clay, are denoted by Ω_c and Ω_s, respectively. The stress and strain increments of the homogenised material ($\mathbf{\Delta\sigma^{eq}}$ and $\mathbf{\Delta\varepsilon^{eq}}$) are computed by using Ω_c and Ω_s (refer to Eq. (5)). The subscripts of c and s indicate the column and soft clay, respectively. The stiffness matrices of the constituents are denoted as $\mathbf{D^c}$ and $\mathbf{D^s}$, respectively.

The strain increment of the homogenised material can be established in terms of the strain increments in the clay and columns, considering the volume fraction of each constituent in Eqs. (18)–(19). When the stress increments in homogenised media are expressed in terms of effective stresses, the ratio of the clay and column strain increments to the equivalent strain increment can be incorporated into formulae using the structural matrices $\mathbf{S^s_1}$ and $\mathbf{S^{s,c}_1}$ as a function of Ω_s, Ω_c, $\mathbf{D^s}$ and $\mathbf{D^c}$ (Eq. (20), for details see Appendix D).

$$(\mathbf{\Delta\sigma^{eq}})' = \mathbf{\Omega_s}(\mathbf{\Delta\sigma^s})' + \mathbf{\Omega_c}(\mathbf{\Delta\sigma^c})' \tag{18}$$

$$\mathbf{D^{eq}\Delta\varepsilon^{eq}} = \mathbf{\Omega_s D^s \Delta\varepsilon^s} + \mathbf{\Omega_c D^c \Delta\varepsilon^c} \tag{19}$$

$$\mathbf{D^{eq}\Delta\varepsilon^{eq}} = \mathbf{\Omega_s D^s S^s_1 \Delta\varepsilon^{eq}} + \mathbf{\Omega_c D^c S^c_1 \Delta\varepsilon^{eq}} \tag{20}$$

Consequently, the generalised expression for the equivalent stiffness matrix $\mathbf{D^{eq}}$ yields Eq. (21).

$$\mathbf{D^{eq}} = \Omega_s D^s S^s_1 + \Omega_c D^c S^c_1 \tag{21}$$

where, the structural matrices $\mathbf{S^s_1}$ and $\mathbf{S^c_1}$ are computed separately to calculate the strain increments of the individual components. The full derivation of the constitutive equations for the equivalent material is presented in Appendix D.

$$\mathbf{S^{c,s}_1} = \begin{bmatrix}1 & 0 & 0 & 0 & 0 & 0\\ 0 & 1 & 0 & 0 & 0 & 0\\ S_{31} & S_{32} & S_{33} & S_{34} & S_{35} & S_{36}\\ 0 & 0 & 0 & 1 & 0 & 0\\ S_{51} & S_{52} & S_{53} & S_{54} & S_{55} & S_{56}\\ S_{61} & S_{62} & S_{63} & S_{64} & S_{65} & S_{66}\end{bmatrix} \tag{22}$$

3.1. Numerical scheme of the volume averaging technique

The volume averaging technique (VAT) was implemented into the PLAXIS 2D FE code as a user-defined soil model (UDSM). Initially, $\mathbf{D^{eq}}$ of the averaged material is established based on the analytical expression in Eq. (21) using the elastic parameters specified by the MNhard and S-CLAY1S models for the column and clay materials, respectively. Subsequently, the finite element code assembles the global elastic material stiffness matrix ($\mathbf{K_E}$) and computes the incremental nodal displacement vector over the whole discretised volume ($\mathbf{\Delta u}$) based on the incremental nodal load vector ($\mathbf{\Delta R_E}$). Utilising the derivatives of the shape functions (**B**), the strain increment vector ($\mathbf{\Delta\varepsilon}$) of the averaged material is then calculated at Gauss points.

After determining the strain increment acting on the overall homogenised material, it is further decomposed into a column strain increment ($\mathbf{\Delta\varepsilon^c}$) and a soft clay strain increment ($\mathbf{\Delta\varepsilon^s}$). The subdivision operates under the assumption of perfect elasticity, using the structural matrices $\mathbf{S^s_1}$ and $\mathbf{S^c_1}$, in Eq. (21). These are assembled assuming elastic material response ($\mathbf{D^s}$ and $\mathbf{D^c}$). Following the strain increment subdivision, the stress integration routines of the S-CLAY1S and MNhard models are called to calculate the corresponding stress increments in the natural clay and mixed columns, respectively. Both models are implemented using standard return mapping schemes (Sloan, 1987; Borst and Heeres, 2002). The implementation in this paper follows the ideas in Vogler (2009). However, the stress corrections in the return algorithm had to be reformulated to incorporate the stress–strain distributions of the individual materials for the case of a braced excavation, instead of an embankment problem, as illustrated in Fig. 9.

Upon the computation of the stress increments, the local equilibrium as introduced in Section 2.2 is checked. If equilibrium is achieved, the effective stress and state parameters of the equivalent material are stored as the updated stress state by the PLAXIS calculation kernel. However, if equilibrium is not achieved, all state variables and stress states revert to their previous values, initiating a subiteration scheme. The scheme involves calling both material routines again with different strain increments. Thereafter, to impose the local equilibrium identified in the 3D analysis, the stress difference between the column and clay is added to the column material. The procedure is illustrated in Fig. 9.

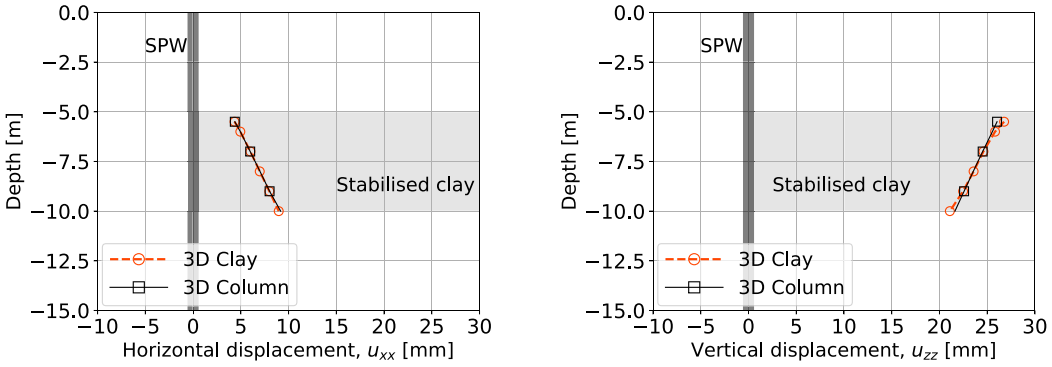

Fig. 8. Comparison of the displacement profiles in the clay and column materials at the final excavation stage along the depths between −5 to −10: (a) horizontal displacements; (b) vertical displacements.

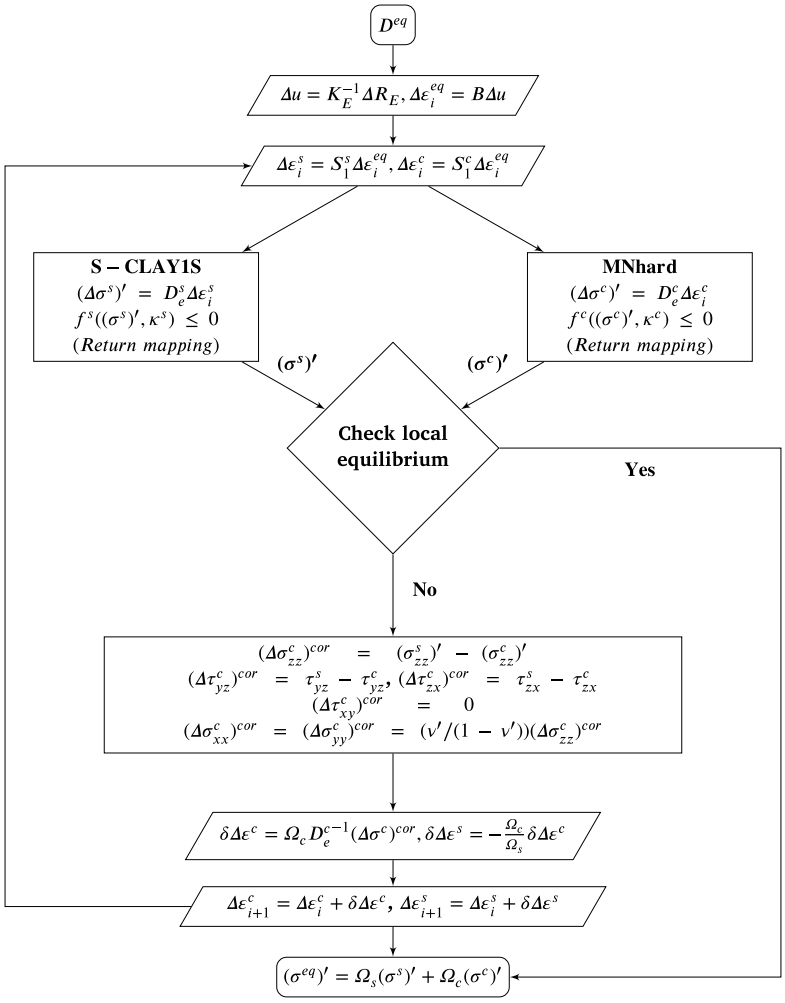

Fig. 9. Solution routine of VAT.

Initially, the out-of-balance stress, $(\Delta\sigma)^{cor}$, causing equilibrium violation, is computed to restore local balance in the z, yz, and zx directions, as described in Eqs. (23).

$$(\Delta\sigma^{c}_{zz})^{cor} = (\sigma^{s}_{zz})' - (\sigma^{c}_{zz})'$$
$$(\Delta\tau^{c}_{yz})^{cor} = (\tau^{s}_{yz}) - (\tau^{c}_{yz}) \quad (23)$$
$$(\Delta\tau^{c}_{zx})^{cor} = (\tau^{s}_{zx}) - (\tau^{c}_{zx})$$

The stresses in the x- and *y*-directions within the two individual materials are independent. However, recovering the stress state in the out-of-plane direction (z) necessitates correcting the stresses in the horizontal (x) and vertical (y) directions. Given the strain equality in the *x* and *y* axes, the 6*6 compliance matrix yields a stress correction of the same magnitude. The correction in the *x* and *y* directions can be achieved by scaling the component in the *z*-direction by $(\frac{\nu'}{1-\nu'})$, where ν' is the Poisson's ratio of the column material. The scaling serves as an approximation in the calculation of the balance equations, therefore using ν' of clay instead would not affect the results.

$$(\Delta\sigma^{c}_{xx})^{cor} = (\Delta\sigma^{c}_{yy})^{cor} = (\nu'/(1-\nu'))(\Delta\sigma^{c}_{zz})^{cor} \quad (24)$$

The individual components of $(\Delta\sigma)^{cor}$ are linked to the strain increments of individual materials. The strain equality in the xy direction implies that $(\Delta\tau_{xy})^{cor}$ should remain unchanged. Finally, the remaining correction stress component is given in Eq. (25).

$$(\Delta\tau^{c}_{xy})^{cor} = 0 \quad (25)$$

The respective volume fractions of Ω_s and Ω_c are employed to apportion the stress difference to the clay and column materials. The total stress increment applied upon the equivalent material remains equal to that of the individual materials in the z, yz, and zx directions. Thus, adjusting the strain increments in these directions within each material, $\Delta\epsilon^{c}$ and $\Delta\epsilon^{s}$, is achieved using the elastic compliance matrix of the column material through Eqs. (26)–(28).

$$\Omega_s\Delta\epsilon^{s} + \Omega_c\Delta\epsilon^{c} = 0 \quad (26)$$

$$\Delta\epsilon^{c} = \Omega_c D_e^{c\,-1}(\Delta\sigma^{c})^{cor} \quad (27)$$

$$\Delta\epsilon^{s} = -\frac{\Omega_c}{\Omega_s}\Delta\epsilon^{c} \quad (28)$$

The correction of the stresses is incorporated into the strain increments of both materials for the subsequent internal iteration, and the individual constitutive laws for both materials are invoked. The averaging scheme leads to the convergence of the stress state of the two constituents towards internal equilibrium in the subsequent iterations. The solution routine ensures the satisfaction of the kinematic conditions and maintains local equilibrium throughout the entire volume averaging process.

4. Verification of the homogenisation technique

The performance of VAT as implemented above is verified by simulating the deep excavation stabilised with deep-mixed columns for plane strain conditions. The 2D FE simulation using VAT produces a final mesh comprising 1138 15-noded triangular elements, totalling 9382 nodes. Each element incorporates 12 Gaussian integration points.

To examine the response of the stabilised clay, the stress–strain distribution of the clay/column system was investigated using discrete columns in the 3D model, while in the 2D plane strain analysis VAT was employed. Sampling points were chosen from comparable locations in the final excavation stage for both simulations (see Fig. 4), following the same construction schedule (see Table 1). The resulting stress–strain distribution of the individual materials, calculated by the 2D analysis, was then compared to that of the 3D analysis. Furthermore, the predicted horizontal displacements of the SPW and the displacements in the excavation area computed by the 2D and 3D analyses were also examined.

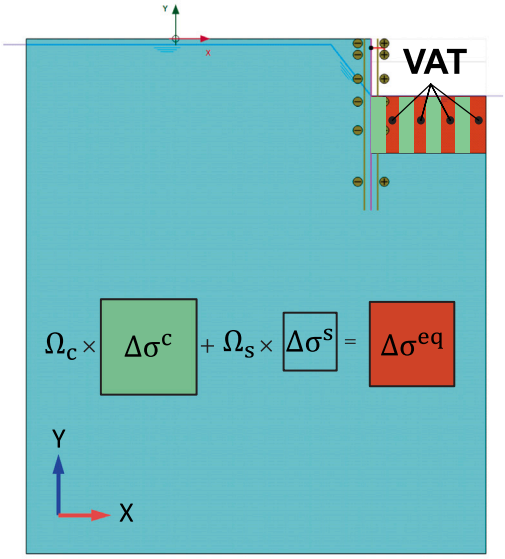

Fig. 10. 2D numerical model of a deep excavation with VAT.

In Figs. 1 and 4, the dimensions of the 3D model are provided; the excavation has a width of 10 m and a length of 14.25 m. Additionally, there is a repeating pattern of 70 cm diameter columns with a 20 m overlap that form a square grid with outer and inner dimensions of 2.5 m and 1.3 m, respectively.

In the 2D simulation to represent the stabilised clay, two regions are defined based on the overlapping LC column arrangement in the out-of-plane direction (refer to Figs. 1 and 10). VAT is utilised in specific regions where both the clay and column materials co-exist, based on the 3D model. The volume fraction of the columns, Ω_c in zones due to the mutual existence of the clay and column materials corresponds to 0.64 ($\Omega_c = (14.25 \times 1.3 - 4 \times 1.3^2)/(14.25 \times 1.3)$). In contrast, in regions where the LC columns are the only material present in the out-of-plane direction, the MNhard model was used to represent the whole region. These two regions in the 2D simulation are illustrated in Fig. 10.

A comparison between the 2D and 3D simulations was made using the 3D global coordinate system, where the axis definitions in the 2D analysis by PLAXIS were inverted to ensure consistency (see Fig. 11). In Fig. 11, *x* and *y* define the horizontal directions, while z represents the vertical direction. The effective stresses in the horizontal (in-plane) and vertical directions were averaged within the column and *in situ* clay materials based on their fractions, as shown in Figs. 11(a) and 11(c). In 2D plane strain conditions, shear stresses in the out-of-plane direction correspond to zero; therefore, the stress equality can be captured only in the out-of-plane direction for the 2D simulation. The stress equality obtained through the 2D analysis using VAT is in good agreement with the 3D analysis, as can be seen in Fig. 11(b). The minor differences in stresses computed between the 2D and 3D simulations result from stress interpolation (from Gauss points in different locations in 2D and 3D), and are expected particularly near material transition zones with differing element stiffness matrices.

The horizontal and vertical displacements in the stabilised excavation area were compared between the 2D and 3D simulations in the final excavation stage. The displacement contours calculated by the 2D simulation using VAT, along with those from the 3D simulation, can be

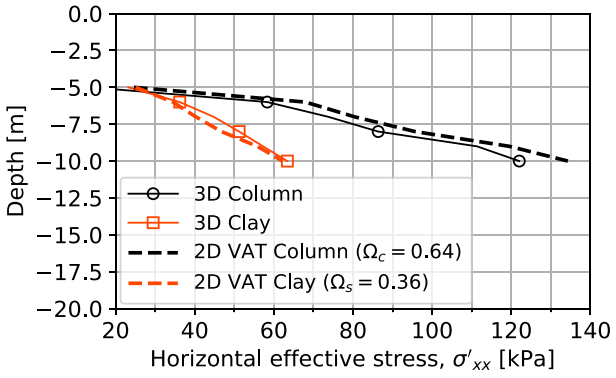

(a)

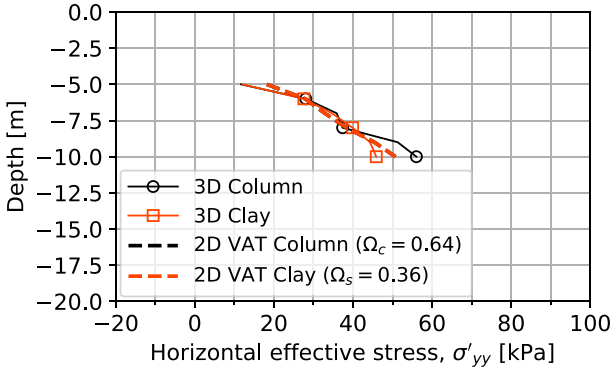

(b)

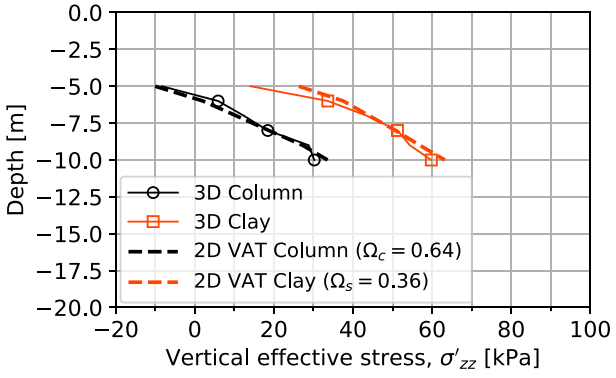

(c)

Fig. 11. Comparison of the stress distribution within the column and clay materials in the 2D and 3D simulations in the final excavation stage: (a) horizontal effective stress, σ'_{xx} in plane axis; (b) horizontal effective stress in the out-of-plane, σ'_{yy}; (c) vertical effective stress, σ'_{zz}.

seen in Figs. 12(a)–12(d). The horizontal displacements computed from the 2D and 3D simulations are of the same order (depicted in Figs. 12(a) and 12(c)), with a maximum horizontal displacement of 13 mm. The maximum vertical displacement computed by the 2D simulation is approximately 32 mm (in Fig. 12(d)), whereas the 3D simulation yields a slightly higher maximum heave, approximately 35 mm (in Fig. 12(b)).

Additionally, the displacement profile of the SPW predicted by the 2D simulation using VAT was compared to the results of the 3D simulation (Figs. 13(a) and 13(b)). Achieving an identical displacement profile between 2D and 3D simulations is highly unlikely. While the 2D analysis using VAT resulted in a marginally smaller maximum heave than the 3D simulation, the method yielded stress and horizontal displacement profiles that closely resemble the 3D results, thus demonstrating that the method is capable of modelling the system performance in Serviceability Limit State.

All analyses were performed on a standard laptop PC with an i5-1345U processor, frequency of 1.2/4.7 GHz (Base/Turbo), and 16 GB of memory. UDSM routines were coded in Intel® Fortran Compiler. The global nonlinear equations are solved for a default tolerated error of 1% margin PLAXIS Scientific Model (2023). The average computation time for the 3D analysis corresponded to 1.5 h, while the 2D simulation with VAT had a significantly shorter elapsed time of approximately 1 min.

5. Conclusions

A volume averaging technique (VAT) was implemented into PLAXIS 2D finite element code for numerical analysis of deep excavations stabilised with lime-cement (LC) columns in soft clay. The distinct stress–strain responses of the soft clay and the columns were represented through an equivalent material based on the volume fraction of each constituent. The fundamental equations of the equivalent constitutive law were established using strain compatibility and stress equilibrium conditions, identified from a reference case with fully coupled 3D consolidation analysis.

The soft clay was modelled using the anisotropic S-CLAY1S soil model, whereas the columns were simulated using the MNhard model. The stress–strain response of the system of stabilised and natural clay as well as the horizontal displacement profile of the SPW were simulated through the 2D analysis using the VAT. The results of the 2D analysis were verified against the 3D results. Employing the VAT provided a close resemblance to the 3D model in terms of quantifying the stresses and displacements within the stabilised region, with good agreement in the displacement profile of the SPW. Thus, the system response was well captured with a fast 2D simulation.

The VAT has proven to be a powerful tool for the numerical analysis of stabilised deep excavations with a significant number of columns installed in a periodic grid pattern. By employing this technique, it becomes possible to capture 3D effects in a 2D plane strain analysis. The proposed method eliminates the need to use numerous soil clusters, thereby reducing the computational cost associated with discretising the geometry. Consequently, the VAT enables efficient incorporation of sensitivity analyses.

The current implementation of the VAT relies on the assumption of similar permeability between soft clay and LC columns, which is based on field evidence when using the dry soil mixing method in Scandinavian clay (Bozkurt et al., 2023). A potential future extension of the technique could involve accounting for varying hydraulic conductivity in soft clay and deep-mixed columns (Lorenzo and Bergado, 2006; Baker, 2017). The possible installation effects of columnar inclusions cannot be modelled using the technique. However, these effects can be implicitly considered by adjusting the stress–strain state through the application of a prescribed external load or strain Schweiger and Pande (1988), Tornborg et al. (2021), Bozkurt et al. (2023) and/or can be explicitly accounted for by a constitutive soil model that can describe the volume change of deep-mixed columns during installation and curing.

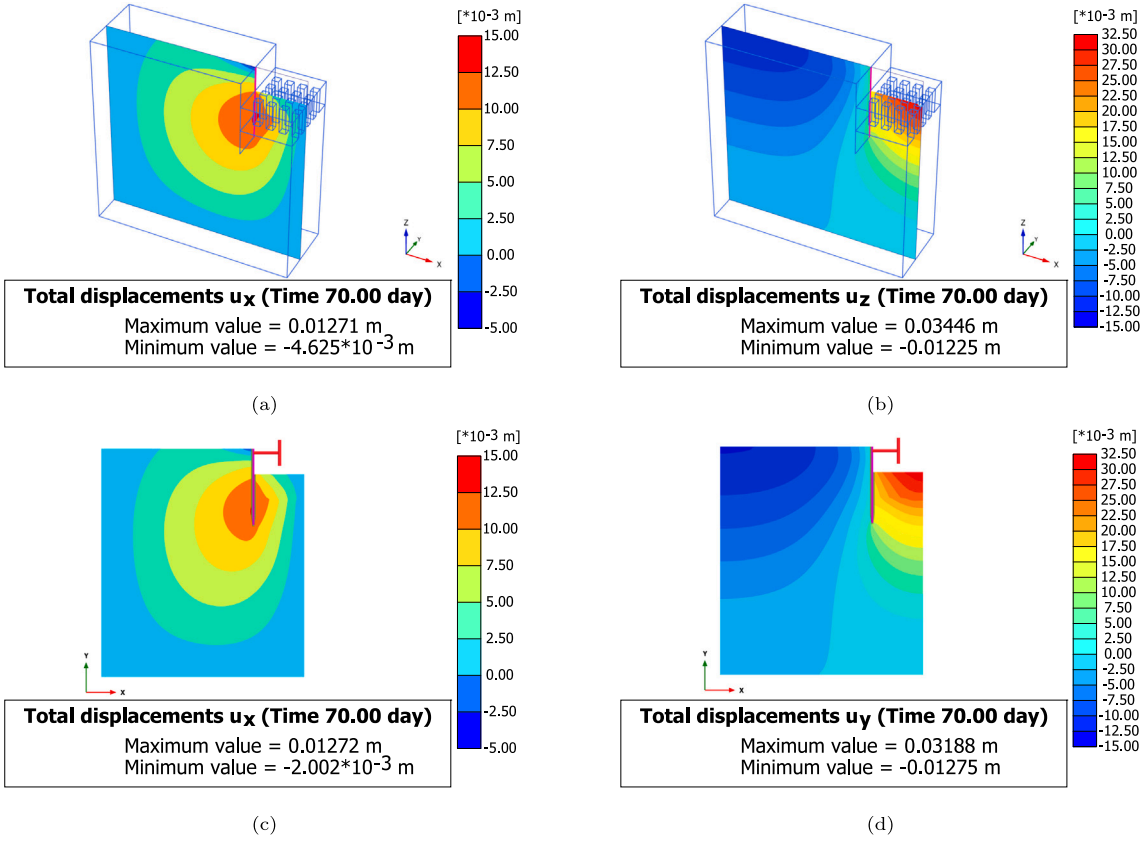

Fig. 12. Displacement contours in the 2D and 3D simulations at the final excavation stage: (a) horizontal displacements, u_x (3D) and (b) vertical displacements, u_z (3D); (c) horizontal displacements, u_x (2D-VAT) and (d) vertical displacements, u_y (2D-VAT).

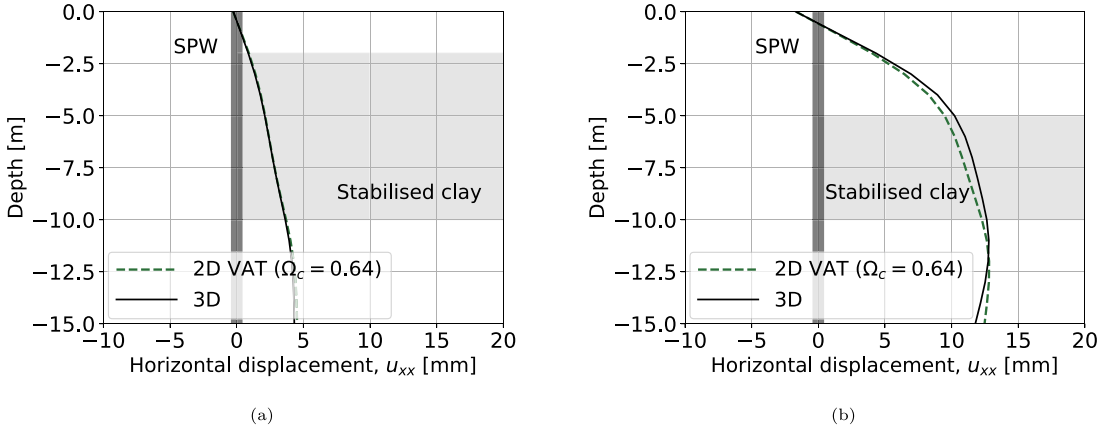

Fig. 13. Comparison of the displacement profiles of the SPW in the 2D and 3D simulations: (a) excavation stage to the level −2; (b) excavation stage to the level −5.

Nomenclature

Abbreviations

CAUC/E	Anisotropically consolidated undrained triaxial compression/extension test
CRS	Constant rate of strain
DSM	Dry soil mixing method
FEA	Finite element analysis
LC	Lime and cement
IL	Incrementally loaded oedometer test
OCR	Overconsolidation ratio
SPW	Sheet pile wall
UDSM	User-defined soil model
VAT	Volume averaging technique

Greek letters

α_0	Initial anisotropy
β	Relative effectiveness of rotational hardening
χ_0	Initial amount of bonding
$\Delta\varepsilon$	Increments of strain
$\Delta\varepsilon^c$	Increments of strain in column material
$\Delta\varepsilon^{eq}$	Increments of strain in equivalent material
$\Delta\varepsilon^s$	Increments of strain in clay material
Δu	Incremental nodal displacement vector
$\Delta\sigma$	Increments of stress
$\Delta\sigma^c$	Increments of stress in column material
$\Delta\sigma^{eq}$	Increments of stress in equivalent material
$\Delta\sigma^s$	Increments of stress in clay material
$(\Delta\sigma)^{cor}$	Out-of-balance stress between clay and columns
γ_s^{ps}	Accumulated deviatoric plastic shear strain
γ_{xy}	Shear total strain on the plane normal to the x-axis in the direction of the y-axis
γ_{yz}	Shear total strain on the plane normal to the y-axis in the direction of the z-axis
γ_{zx}	Shear total strain on the plane normal to the z-axis in the direction of the x-axis
κ	Slope of the swelling line
Λ	Viscoplastic multiplier
λ_i	Slope of the intrinsic normal compression line
μ	Absolute effectiveness of rotational hardening
ν'	Effective Poisson's ratio
Ω_c	Volume fraction of column
Ω_s	Volume fraction of clay
ϕ'	Effective friction angle
σ'_1	Major principal effective stress
σ'_2	Intermediate principal effective stress
σ'_3	Minor principal effective stress
σ'_{xx}	Normal effective stress acting on the x-axis
σ'_{yy}	Normal effective stress acting on the y-axis
σ'_{zz}	Normal effective stress acting on the z-axis
σ'^{ref}	Reference effective stress
τ_{xy}	Shear effective stress on the plane normal to the x-axis in the direction of the y-axis
τ_{yz}	Shear effective stress on the plane normal to the y-axis in the direction of the z-axis
τ_{zx}	Shear effective stress on the plane normal to the z-axis in the direction of the x-axis
ε_1	Major principal total strain
ε_2	Intermediate principal total strain
ε_3	Minor principal total strain
ε_{xx}	Normal total strain acting on the x-axis
ε_{yy}	Normal total strain acting on the y-axis

Greek letters

ε_{zz}	Normal total strain acting on the z-axis
ε_v^e	Elastic volumetric strain
ε_d^p	Plastic deviatoric strain
ε_v^p	Plastic volumetric strain

Miscellaneous

$\langle\rangle$	Macaulay brackets

Roman capital letters

B	Shape function
D	Elastic constitutive matrix
D^c	Elastic constitutive matrix of column material
D^{eq}	Elastic constitutive matrix of equivalent material
D^s	Elastic constitutive matrix of clay material
E'_{50}	Secant stiffness
E'_{ur}	Unloading reloading stiffness
G	Shear stress
G_{50}^{ref}	Reference secant shear stress
G_{ur}^{ref}	Reference unloading reloading shear stress
K_0	Coefficient of earth pressure
K_E	Global elastic material stiffness matrix
M	Stress ratio at critical state
R_E	Nodal load vector
R_f	Failure ratio of deviatoric stress
S_1	Strain redistribution matrix
S_s	Structural matrix

Roman lower case letters

a	Absolute rate of destructuration due to volumetric strain
b	Relative rate of destructuration due to volumetric strain
c	Notation for column material
c'	Effective cohesion
c_k	Permeability change index
e_0	Initial void ratio
eq	Notation for equivalent material
k	Hydraulic conductivity
m	Extent of stiffness dependency
p'	Mean effective stress
p'_m	Initial mean effective stress at preconsolidation pressure
p'_{mi}	Size of the intrinsic yield surface
q	Deviatoric stress
q_a	Asymptotic deviatoric stress
q_f	Deviatoric stress at failure
r_c	Column radius
s	Notation for clay material
s_c	Column spacing

CRediT authorship contribution statement

Sinem Bozkurt: Writing – original draft, Visualization, Software, Methodology, Formal analysis, Conceptualization. **Ayman Abed:** Writing – review & editing, Supervision. **Minna Karstunen:** Writing – review & editing, Supervision.

Declaration of competing interest

The authors declare that they have no known competing financial interests or personal relationships that could have appeared to influence the work reported in this paper.

Acknowledgements

The work received financial support from BIG (Better Interaction in Geotechnics, Grants TRV2020/46703 and TRV 2024/27461) through the Swedish Transport Administration (TRV) and Formas (Grant 2019-00456). The work is done as a part of the Digital Twin Cities Centre that is supported by Sweden's Innovation Agency VINNOVA (Grants 2019-00041 and 2024-03904). The authors also wish to express their gratitude to NCC AB for providing access to the field measurements.

Appendix A. S-CLAY1S model

The generalised formulation of the S-CLAY1S model (Koskinen et al., 2002; Karstunen et al., 2005) in 3D stress space can be expressed by using the following definitions. The yield surface equation in triaxial stress space is given in Section 2.1.

$$f_{3D} = \underbrace{\frac{3}{2}\left(\{\sigma'_d - p'\alpha_d\}^T\{\sigma'_d - p'\alpha_d\}\right)}_{q^2} - \left(M^2 - \underbrace{\frac{3}{2}\{\alpha_d\}^T\{\alpha_d\}}_{\alpha^2}\right)\times$$
$$\left(p'_m - p'\right)p' = 0 \tag{A.1}$$

where $q^2 = 3/2\left(\{\sigma'_d - p'\alpha_d\}^T\{\sigma'_d - p'\alpha_d\}\right)$ is the scalar value of the modified deviatoric stress tensor, including anisotropy represented by a deviatoric fabric tensor α_d. $q = (\sigma'_1 - \sigma'_3)$ in triaxial stress space. Mean effective stress is $p' = (\sigma'_1 + \sigma'_2 + \sigma'_3)/3$ and the vertical tangent to natural yield surface designates the size in the isotropic axis, p'_m. M represents the stress ratio at the critical state. The subscript scalar value of the fabric tensor denotes α defined as $\alpha^2 = 3/2\left({\alpha_d}^T : \alpha_d\right)$, which describes the orientation of the model surfaces, as illustrated in triaxial stress space in Fig. 2. The deviatoric stress tensor and deviatoric fabric tensor are expressed by Eqs. (A.2) and (A.3).

$$\sigma'_d = \begin{bmatrix} \sigma'_x - p' \\ \sigma'_y - p' \\ \sigma'_z - p' \\ \sqrt{2}\tau_{xy} \\ \sqrt{2}\tau_{yz} \\ \sqrt{2}\tau_{zx} \end{bmatrix} \tag{A.2}$$

$$\alpha_d = \begin{bmatrix} \frac{1}{3}\left(2\alpha_x - \alpha_y - \alpha_z\right) \\ \frac{1}{3}\left(-\alpha_x + 2\alpha_y - \alpha_z\right) \\ \frac{1}{3}\left(-\alpha_x - \alpha_y + 2\alpha_z\right) \\ \sqrt{2}\alpha_{xy} \\ \sqrt{2}\alpha_{yz} \\ \sqrt{2}\alpha_{zx} \end{bmatrix} \text{with } \frac{1}{3}\left(\alpha_x + \alpha_y + \alpha_z\right) = 1 \tag{A.3}$$

Deviatoric and volumetric components of elastic strains can be computed as follows:

$$\Delta{\varepsilon_v}^e = \frac{\kappa}{(1+e)p'}\Delta p' \text{ and } \Delta{\varepsilon_q}^e = \frac{1}{3G}\Delta q \tag{A.4}$$

Deviatoric and volumetric components of plastic strains can be computed using the flow rule. For associated plasticity, the yield function coincides with the plastic potential, thus.

$$\Delta{\varepsilon_v}^p = \Delta\Lambda\frac{\partial f}{\partial p'} \text{ and } \Delta{\varepsilon_q}^p = \Delta\Lambda\frac{\partial f}{\partial q} \tag{A.5}$$

The size of the intrinsic yield surface is assumed to be dependent only on volumetric plastic strains, ε_v^p.

$$\Delta p'_{mi} = \frac{(1+e)\,p'_{mi}}{\lambda_i - \kappa}\Delta\varepsilon_v^p \tag{A.6}$$

The evolution of the size of p'_m, corresponding to the current degree of bonding (χ), and the degradation of bonding are calculated with Eq. (A.7). The Macaulay brackets, $\langle\rangle$ are used to impose $\Delta\varepsilon_v^p = \Delta\varepsilon_v^p$ for $\Delta\varepsilon_v^p > 0$ and $\Delta\varepsilon_v^p = 0$ for $\Delta\varepsilon_v^p < 0$.

$$\Delta\chi = -a\chi\left(\langle\Delta\varepsilon_v^p\rangle + b\Delta\varepsilon_d^p\right) \text{ and } {p'}_m = (p'_{mi} + \Delta p'_{mi})(1 + (\chi + \Delta\chi)) \tag{A.7}$$

The evolution of anisotropy is described with Eq. (A.8) in 3D stress space.

$$\Delta\alpha = \mu\left[\left(\frac{3\sigma'_d}{4p'} - \alpha_d\right)\left\langle\Delta\varepsilon_v^p\right\rangle + \beta\left(\frac{\sigma'_d}{3p'} - \alpha_d\right)\Delta\varepsilon_d^p\right] \tag{A.8}$$

Appendix B. MNhard model

The MNhard soil model (Benz, 2007) utilises shear hardening only. The yield surface equation is given in Eq. (B.1). γ_s^{ps} is the hardening parameter and the plastic part of the objective shear strain measure ($\gamma^{ps} = \sqrt{\frac{1}{2}((\varepsilon_1 - \varepsilon_2)^2 + (\varepsilon_2 - \varepsilon_3)^2 + (\varepsilon_3 - \varepsilon_1)^2)}$).

$$f_s = \frac{3}{4}\frac{q}{E'_{50}}\frac{\frac{1-\sin\phi_m}{\sin\phi_m}}{\frac{1-\sin\phi_m}{\sin\phi_m} - R_f\frac{1-\sin\phi}{\sin\phi}} - \frac{3}{2}\frac{2q}{E'_{ur}} - \gamma_s^{ps} \text{ and } R_f = \frac{q_f}{q_a} < 1.0 \tag{B.1}$$

The cone hardening functions can be written using the MNhard yield criterion. Upon reaching the failure condition, the ratio of shear stress to mean effective stress corresponds to the limiting value in Eq. (B.2).

$$sin\phi'_m = \sqrt{\frac{9 - \frac{I_1 I_2}{I_3}}{1 - \frac{I_1 I_2}{I_3}}} \tag{B.2}$$

The first, second, and third effective stress invariants are represented by I_1, I_2, and I_3, respectively (in Eq. (B.3)).

$$\begin{aligned} I_1 &= \sigma_{ii} \\ I_2 &= \frac{1}{2}\left(\sigma_{ij}\sigma_{ij} - \sigma_{ii}\sigma_{jj}\right) \\ I_3 &= \frac{1}{6}\left(\sigma_{ii}\sigma_{jj}\sigma_{kk} + 2\sigma_{ij}\sigma_{jk}\sigma_{ki} - 3\sigma_{ij}\sigma_{ji}\sigma_{kk}\right) \end{aligned} \tag{B.3}$$

The plastic potential to the cone-type yield surface is defined using Eq. (B.4) with a non-associated flow rule.

$$g = (p + c\cot\psi)\frac{6\sin\psi_m}{3 - sin\psi_m} \tag{B.4}$$

where,

$$\sin\psi'_m = \frac{\sin\phi'_m - \sin\phi'_{cv}}{1 - \sin\phi'_m\sin\phi'_{cv}} \geq 0 \tag{B.5}$$

$$\sin\phi'_{cv} = \frac{\sin\phi' - \sin\psi}{1 - \sin\phi'\sin\psi} \tag{B.6}$$

Appendix C. Calibration of soil model parameters of soft clay

The S-CLAY1S soil model parameters were calibrated using high-quality laboratory testing data obtained from a temporary excavation site in Gothenburg, as described in Bozkurt et al. (2023). In the reference study, the model parameters of the soft clay were simulated using Creep S-CLAY1S model. In this study, the calibration of the S-CLAY1S model parameters using CADE and IL tests was carried out through the single-point Gauss integration via the SoilTest facility in the PLAXIS 2D FE code. Procedures proposed in Gras et al. (2017, 2018) were followed, thus first deriving the values for standard parameters from fall cone (sensitivity for initial amount of bonding), oedometer and triaxial tests, and using the ranges proposed by Gras et al. (2018) for the non-standard parameters, which were then calibrated via lab test simulations. The simulation of the laboratory tests can be seen in Figs. C.14 and C.15.

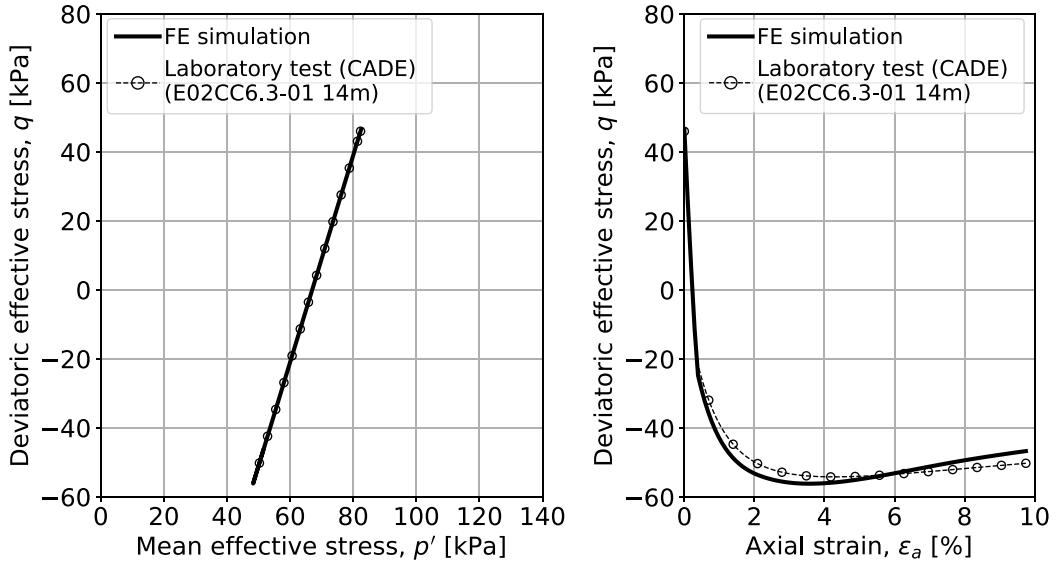

Fig. C.14. Simulation of CADE test using the S-CLAY1S model: (a) deviatoric stress, q and mean effective stress, p′; (b) deviatoric stress, q and axial strain, ε_a.

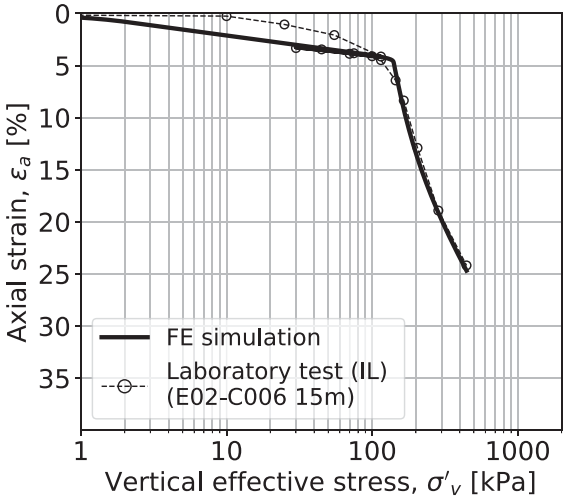

Fig. C.15. Simulation of IL test using the S-CLAY1S model.

Appendix D. Constitutive equations of the equivalent continuum

The continuity of the horizontal stress (in the out-of-plane direction) between the individual materials leads to independent strain distribution. Therefore, substituting compatibility conditions using Eq. (2) into equilibrium conditions (Eqs. (11)–(13)) leads to the following forms.

$$\left(D^s_{33}+D^c_{33}\frac{\Omega_s}{\Omega_c}\right)\Delta\varepsilon^s_z=\left(D^c_{31}-D^s_{31}\right)\Delta\varepsilon^{eq}_x+\left(D^c_{32}-D^s_{32}\right)\Delta\varepsilon^{eq}_y+D^c_{33}\frac{\Delta\varepsilon^{eq}_z}{\Omega_c}+\left(D^c_{34}-D^s_{34}\right)\Delta\gamma^{eq}_{xy}-D^s_{35}\frac{\Delta\gamma^{eq}_{yz}}{\Omega_s}-D^s_{36}\frac{\Delta\gamma^{eq}_{zx}}{\Omega_s}+\left(D^c_{35}+D^s_{35}\frac{\Omega_c}{\Omega_s}\right)\Delta\gamma^c_{yz}+\left(D^c_{36}+D^s_{36}\frac{\Omega_c}{\Omega_s}\right)\Delta\gamma^c_{zx} \tag{D.1}$$

$$\left(D^s_{55}+D^c_{55}\frac{\Omega_s}{\Omega_c}\right)\Delta\gamma^s_{yz}=\left(D^c_{51}-D^s_{51}\right)\Delta\varepsilon^{eq}_x+\left(D^c_{52}-D^s_{52}\right)\Delta\varepsilon^{eq}_y-D^s_{53}\frac{\Delta\varepsilon^{eq}_z}{\Omega_s}+\left(D^c_{54}-D^s_{54}\right)\Delta\gamma^{eq}_{xy}+D^c_{55}\frac{\Delta\gamma^{eq}_{yz}}{\Omega_c}+\left(D^c_{53}+D^s_{53}\frac{\Omega_c}{\Omega_s}\right)\Delta\varepsilon^c_z+\left(D^c_{56}+D^s_{56}\frac{\Omega_c}{\Omega_s}\right)\Delta\gamma^c_{zx}-D^s_{56}\frac{\Delta\gamma^{eq}_{zx}}{\Omega_s} \tag{D.2}$$

$$\left(D^s_{66}+D^c_{66}\frac{\Omega_s}{\Omega_c}\right)\Delta\gamma^s_{zx}=\left(D^c_{61}-D^s_{61}\right)\Delta\varepsilon^{eq}_x+\left(D^c_{62}-D^s_{62}\right)\Delta\varepsilon^{eq}_y-D^s_{63}\frac{\Delta\varepsilon^{eq}_z}{\Omega_s}+\left(D^c_{64}-D^s_{64}\right)\Delta\gamma^{eq}_{xy}-D^c_{65}\frac{\Delta\gamma^{eq}_{yz}}{\Omega_s}+\left(D^c_{63}+D^s_{63}\frac{\Omega_c}{\Omega_s}\right)\Delta\varepsilon^c_z+\left(D^c_{65}+D^s_{65}\frac{\Omega_c}{\Omega_s}\right)\Delta\gamma^c_{yz}+D^c_{66}\frac{\Delta\gamma^{eq}_{zx}}{\Omega_c} \tag{D.3}$$

Through the rearrangement of Eqs. (D.1)–(D.3) into matrix form, the expression in Eq. (D.4) for the *in situ* clay can be obtained.

$$\boldsymbol{\delta\Delta\varepsilon^s}=\boldsymbol{\alpha^s\Delta\varepsilon^{eq}}+\boldsymbol{\beta^s\delta\Delta\varepsilon^c} \tag{D.4}$$

where the matrices of $\boldsymbol{\delta}$, $\boldsymbol{\alpha^s}$, $\boldsymbol{\beta^s}$, and the substituting components of $\mathbf{C_1}$, $\mathbf{C_2}$ and $\mathbf{C_3}$ are computed in Eqs. (D.5)–(D.8), respectively.

$$\boldsymbol{\delta}=\begin{bmatrix}0&0&1&0&0&0\\0&0&0&0&1&0\\0&0&0&0&0&1\end{bmatrix} \tag{D.5}$$

$$\boldsymbol{\alpha^s}=\begin{bmatrix}\frac{D^c_{31}-D^s_{31}}{C_1}&\frac{D^c_{32}-D^s_{32}}{C_1}&\frac{D^c_{33}}{\Omega_cC_1}&\frac{D^c_{34}-D^s_{34}}{C_1}&\frac{-D^s_{35}}{\Omega_sC_1}&\frac{-D^s_{36}}{\Omega_sC_1}\\\frac{D^c_{51}-D^s_{51}}{C_2}&\frac{D^c_{52}-D^s_{52}}{C_2}&\frac{-D^s_{53}}{\Omega_sC_2}&\frac{D^c_{54}-D^s_{54}}{C_2}&\frac{D^c_{55}}{\Omega_cC_2}&\frac{-D^s_{56}}{\Omega_sC_2}\\\frac{D^c_{61}-D^s_{61}}{C_3}&\frac{D^c_{62}-D^s_{62}}{C_3}&\frac{-D^c_{63}}{\Omega_sC_3}&\frac{D^c_{64}-D^s_{64}}{C_3}&\frac{-D^c_{65}}{\Omega_sC_3}&\frac{D^s_{66}}{\Omega_cC_3}\end{bmatrix} \tag{D.6}$$

$$\boldsymbol{\beta^s}=\begin{bmatrix}0&\left(D^c_{35}+D^s_{35}\frac{\Omega_c}{\Omega_s}\right)&\left(D^c_{36}+D^s_{36}\frac{\Omega_c}{\Omega_s}\right)\\\left(D^c_{53}+D^s_{53}\frac{\Omega_c}{\Omega_s}\right)&0&\left(D^c_{56}+D^s_{56}\frac{\Omega_c}{\Omega_s}\right)\\\left(D^c_{63}+D^s_{63}\frac{\Omega_c}{\Omega_s}\right)&\left(D^c_{65}+D^s_{65}\frac{\Omega_c}{\Omega_s}\right)&0\end{bmatrix} \tag{D.7}$$

$$\begin{bmatrix}\mathbf{C_1}\\ \mathbf{C_2}\\ \mathbf{C_3}\end{bmatrix}=\begin{bmatrix}\left(D^s_{33}+D^c_{33}\frac{\Omega_s}{\Omega_c}\right)\\ \left(D^s_{55}+D^c_{55}\frac{\Omega_s}{\Omega_c}\right)\\ \left(D^s_{66}+D^c_{66}\frac{\Omega_s}{\Omega_c}\right)\end{bmatrix} \tag{D.8}$$

Similarly, considering the equal stress distribution between each constituent, varied strain increments in the columns can be calculated using Eqs. (D.9)–(D.11).

$$\left(D^c_{33}+D^s_{33}\frac{\Omega_c}{\Omega_s}\right)\Delta\varepsilon^c_z=\left(D^s_{31}-D^c_{31}\right)\Delta\varepsilon^{eq}_x+\left(D^s_{32}-D^c_{32}\right)\Delta\varepsilon^{eq}_y+D^s_{33}\frac{\Delta\varepsilon^{eq}_z}{\Omega_s}+\left(D^s_{34}-D^c_{34}\right)\Delta\gamma^{eq}_{xy}-D^c_{35}\frac{\Delta\gamma^{eq}_{yz}}{\Omega_c}-D^c_{36}\frac{\Delta\gamma^{eq}_{zx}}{\Omega_c}+\left(D^s_{35}+D^c_{35}\frac{\Omega_s}{\Omega_c}\right)\Delta\gamma^s_{yz}+\left(D^s_{36}+D^c_{36}\frac{\Omega_s}{\Omega_c}\right)\Delta\gamma^s_{zx} \tag{D.9}$$

$$\left(D^c_{55}+D^s_{55}\frac{\Omega_c}{\Omega_s}\right)\Delta\gamma^c_{yz}=\left(D^s_{51}-D^c_{51}\right)\Delta\varepsilon^{eq}_x+\left(D^s_{52}-D^c_{52}\right)\Delta\varepsilon^{eq}_y-D^c_{53}\frac{\Delta\varepsilon^{eq}_z}{\Omega_c}+\left(D^s_{54}-D^c_{54}\right)\Delta\gamma^{eq}_{xy}+D^s_{55}\frac{\Delta\gamma^{eq}_{yz}}{\Omega_s}+\left(D^s_{53}+D^c_{53}\frac{\Omega_s}{\Omega_c}\right)\Delta\varepsilon^s_z+\left(D^s_{56}+D^c_{56}\frac{\Omega_s}{\Omega_c}\right)\Delta\gamma^s_{zx}-D^c_{56}\frac{\Delta\gamma^{eq}_{zx}}{\Omega_c} \tag{D.10}$$

$$\left(D^c_{66}+D^s_{66}\frac{\Omega_c}{\Omega_s}\right)\Delta\gamma^c_{zx}=\left(D^s_{61}-D^c_{61}\right)\Delta\varepsilon^{eq}_x+\left(D^s_{62}-D^c_{62}\right)\Delta\varepsilon^{eq}_y-D^c_{63}\frac{\Delta\varepsilon^{eq}_z}{\Omega_c}+\left(D^s_{64}-D^c_{64}\right)\Delta\gamma^{eq}_{xy}-D^s_{65}\frac{\Delta\gamma^{eq}_{yz}}{\Omega_c}+\left(D^s_{63}+D^c_{63}\frac{\Omega_s}{\Omega_c}\right)\Delta\varepsilon^s_z+\left(D^s_{65}+D^c_{65}\frac{\Omega_s}{\Omega_c}\right)\Delta\gamma^s_{yz}+D^s_{66}\frac{\Delta\gamma^{eq}_{zx}}{\Omega_s} \tag{D.11}$$

Rearranging the above equations results in Eq. (D.12) for the columns.

$$\boldsymbol{\delta\Delta\varepsilon^c}=\boldsymbol{\alpha^c\Delta\varepsilon^{eq}}+\boldsymbol{\beta^c\delta\Delta\varepsilon^s} \tag{D.12}$$

The incremental stresses in the columns can be computed using the matrices of $\boldsymbol{\delta}$, $\boldsymbol{\alpha^c}$, $\boldsymbol{\beta^c}$, and the substituting components of $\mathbf{C_4}$, $\mathbf{C_5}$ and $\mathbf{C_6}$ defined as in Eqs. (D.5) and (D.13)–(D.15), respectively.

$$\boldsymbol{\alpha^c}=\begin{bmatrix}\frac{D^s_{31}-D^c_{31}}{C_4} & \frac{D^s_{32}-D^c_{32}}{C_4} & \frac{D^s_{33}}{\Omega_sC_4} & \frac{D^s_{34}-D^c_{34}}{C_4} & \frac{-D^c_{35}}{\Omega_cC_4} & \frac{-D^c_{36}}{\Omega_cC_4}\\ \frac{D^s_{51}-D^c_{51}}{C_5} & \frac{D^s_{52}-D^c_{52}}{C_5} & \frac{-D^c_{53}}{\Omega_cC_5} & \frac{D^s_{54}-D^c_{54}}{C_5} & \frac{D^s_{55}}{\Omega_sC_5} & \frac{-D^c_{56}}{\Omega_cC_5}\\ \frac{D^s_{61}-D^c_{61}}{C_6} & \frac{D^s_{62}-D^c_{62}}{C_6} & \frac{-D^s_{63}}{\Omega_cC_6} & \frac{D^s_{64}-D^c_{64}}{C_6} & \frac{-D^c_{65}}{\Omega_cC_6} & \frac{D^c_{66}}{\Omega_sC_6}\end{bmatrix} \tag{D.13}$$

$$\boldsymbol{\beta^c}=\begin{bmatrix}0 & \left(D^s_{35}+D^c_{35}\frac{\Omega_s}{\Omega_c}\right) & \left(D^s_{36}+D^c_{36}\frac{\Omega_s}{\Omega_c}\right)\\ \left(D^s_{53}+D^c_{53}\frac{\Omega_s}{\Omega_c}\right) & 0 & \left(D^s_{56}+D^c_{56}\frac{\Omega_s}{\Omega_c}\right)\\ \left(D^s_{63}+D^c_{63}\frac{\Omega_s}{\Omega_c}\right) & \left(D^s_{65}+D^c_{65}\frac{\Omega_s}{\Omega_c}\right) & 0\end{bmatrix} \tag{D.14}$$

$$\begin{bmatrix}\mathbf{C_4}\\ \mathbf{C_5}\\ \mathbf{C_6}\end{bmatrix}=\begin{bmatrix}\left(D^c_{33}+D^s_{33}\frac{\Omega_c}{\Omega_s}\right)\\ \left(D^c_{55}+D^s_{55}\frac{\Omega_c}{\Omega_s}\right)\\ \left(D^c_{66}+D^s_{66}\frac{\Omega_c}{\Omega_s}\right)\end{bmatrix} \tag{D.15}$$

Substituting Eq. (D.12) into (D.4) leads to the expression relating the homogenised material strain and *in situ* clay strain.

$$\boldsymbol{\delta\Delta\varepsilon^s}=\boldsymbol{\alpha^s\Delta\varepsilon^{eq}}+\boldsymbol{\beta^s\alpha^c\Delta\varepsilon^{eq}}+\boldsymbol{\beta^s\beta^c\delta\Delta\varepsilon^s} \tag{D.16}$$

Eq. (D.16) can be simplified to Eqs. (D.17)–(D.18) using the 3*3 unity matrix **I**.

$$\boldsymbol{\delta\Delta\varepsilon^s}=\underbrace{\left(\mathbf{I}-\boldsymbol{\beta^s\beta^c}\right)^{-1}\left(\boldsymbol{\alpha^s}+\boldsymbol{\beta^s\alpha^c}\right)}_{\boldsymbol{S^s}}\boldsymbol{\Delta\varepsilon^{eq}} \tag{D.17}$$

$$\boldsymbol{\delta\Delta\varepsilon^s}=\mathbf{S^s}\boldsymbol{\Delta\varepsilon^{eq}} \tag{D.18}$$

The strain increments in the clay can then be expressed by Eq. (D.19), using the strain redistribution matrix, $\mathbf{S^s_1}$ (Eq. (D.20)), substituting $\mathbf{S^s}$.

$$\boldsymbol{\Delta\varepsilon^s}=\mathbf{S^s_1}\boldsymbol{\Delta\varepsilon^{eq}} \tag{D.19}$$

where,

$$\mathbf{S^s_1}=\begin{bmatrix}1 & 0 & 0 & 0 & 0 & 0\\ 0 & 1 & 0 & 0 & 0 & 0\\ S_{31} & S_{32} & S_{33} & S_{34} & S_{35} & S_{36}\\ 0 & 0 & 0 & 1 & 0 & 0\\ S_{51} & S_{52} & S_{53} & S_{54} & S_{55} & S_{56}\\ S_{61} & S_{62} & S_{63} & S_{64} & S_{65} & S_{66}\end{bmatrix} \tag{D.20}$$

An analogous relation can be derived but for the incremental strains in the columns through Eqs. (D.21)–(D.25).

$$\boldsymbol{\delta\Delta\varepsilon^c}=\boldsymbol{\alpha^c\Delta\varepsilon^{eq}}+\boldsymbol{\beta^c\alpha^s\Delta\varepsilon^{eq}}+\boldsymbol{\beta^c\beta^s\delta\Delta\varepsilon^c} \tag{D.21}$$

$$\boldsymbol{\delta\Delta\varepsilon^c}=\underbrace{\left(\mathbf{I}-\boldsymbol{\beta^s\beta^c}\right)^{-1}\left(\boldsymbol{\alpha^c}+\boldsymbol{\beta^c\alpha^s}\right)}_{\boldsymbol{S^c}}\boldsymbol{\Delta\varepsilon^{eq}} \tag{D.22}$$

$$\boldsymbol{\delta\Delta\varepsilon^c}=\mathbf{S^c}\boldsymbol{\Delta\varepsilon^{eq}} \tag{D.23}$$

$$\boldsymbol{\Delta\varepsilon^c}=\mathbf{S^c_1}\boldsymbol{\Delta\varepsilon^{eq}} \tag{D.24}$$

where,

$$\mathbf{S^c_1}=\begin{bmatrix}1 & 0 & 0 & 0 & 0 & 0\\ 0 & 1 & 0 & 0 & 0 & 0\\ S_{31} & S_{32} & S_{33} & S_{34} & S_{35} & S_{36}\\ 0 & 0 & 0 & 1 & 0 & 0\\ S_{51} & S_{52} & S_{53} & S_{54} & S_{55} & S_{56}\\ S_{61} & S_{62} & S_{63} & S_{64} & S_{65} & S_{66}\end{bmatrix} \tag{D.25}$$

Data availability

Data will be made available on request.

References

Anglade, E., Sellier, A., Papon, A., Aubert, J.E., 2023. Homogenization with non-homogeneous plastic flow. Int. J. Numer. Anal. Methods Geomech. http://dx.doi.org/10.1002/NAG.3616.

Baker, S., 2017. Three dimensional consolidation settlement of stabilized soil using lime/cement columns. In: Dry Mix Methods for Deep Soil Stabilization. Routledge, pp. 207–214.

Benz, T., 2007. Small-Strain Stiffness of Soils and Its Numerical Consequences (Ph.D. thesis). Mitteilung 55 des Institutsfür Geotechnik, Universität Stuttgart.

Benz, T., Wehnert, M., Vermeer, P.A., 2008. A lode angle dependent formulation of the hardening soil model. In: 12th International Conference on Computer Methods and Advances in Geomechanics. Vol. 2008, pp. 653–660.

Bharali, R., Larsson, F., Jänicke, R., 2021. Computational homogenisation of phase-field fracture. Eur. J. Mech. A Solids 88, 104247. http://dx.doi.org/10.1016/j.euromechsol.2021.104247.

Borst, R.D., Heeres, O.M., 2002. A unified approach to the implicit integration of standard, non-standard and viscous plasticity models. Int. J. Numer. Anal. Methods Geomech. 26, 1059–1070. http://dx.doi.org/10.1002/NAG.234.

Bozkurt, S., Abed, A., Karstunen, M., 2023. Finite element analysis for a deep excavation in soft clay supported by lime-cement columns. Comput. Geotech. 162, 105687. http://dx.doi.org/10.1016/j.compgeo.2023.105687.

Canetta, G., Nova, R., 1989. A numerical method for the analysis of ground improved by columnar inclusions. Comput. Geotech. 7, 99–114. http://dx.doi.org/10.1016/0266-352X(89)90009-8.

Dvorak, G., Bahei-El-Din, Y., 1979. Elastic–plastic behavior of fibrous composites. J. Mech. Phys. Solids 27, 51–72. http://dx.doi.org/10.1016/0022-5096(79)90010-3.

Dvorak, G.J., Zhang, J., 2001. Transformation field analysis of damage evolution in composite materials. J. Mech. Phys. Solids 49, 2517–2541. http://dx.doi.org/10.1016/S0022-5096(01)00066-7.

Finno, R.J., Blackburn, J.T., Roboski, J.F., 2007. Three-dimensional effects for supported excavations in clay. J. Geotech. Geoenviron. Eng. 133, 30–36. http://dx.doi.org/10.1061/(ASCE)1090-0241(2007)133:1(30).

Gens, A., Nova, R., 1993. Conceptual bases for a constitutive model for bonded soils and weak rocks. Geotech. Eng. Hard Soils – Soft Rocks 485–494.

Gras, J.P., Sivasithamparam, N., Karstunen, M., Dijkstra, J., 2017. Strategy for consistent model parameter calibration for soft soils using multi-objective optimisation. Comput. Geotech. 90, 164–175. http://dx.doi.org/10.1016/J.COMPGEO.2017.06.006.

Gras, J.P., Sivasithamparam, N., Karstunen, M., Dijkstra, J., 2018. Permissible range of model parameters for natural fine-grained materials. Acta Geotech. 13, 387–398. http://dx.doi.org/10.1007/S11440-017-0553-1.

Hashin, Z., 1983. Analysis of composite materials—A survey. J. Appl. Mech. 50, 481–505. http://dx.doi.org/10.1115/1.3167081.

Hill, R., 1963. Elastic properties of reinforced solids: Some theoretical principles. J. Mech. Phys. Solids 11, 357–372. http://dx.doi.org/10.1016/0022-5096(63)90036-X.

Idesman, A.V., Levitas, V.I., Stein, E., 1996. Finite-element simulation of elastoplastic properties of two-phase composites reinforced by particles. In: IUTAM Symposium on Micromechanics of Plasticity and Damage of Multiphase Materials, Springer Netherlands. Dordrecht, pp. 83–90. http://dx.doi.org/10.1007/978-94-009-1756-9_11.

Jellali, B., Bouassida, M., Buhan, P.de., 2005. A homogenization method for estimating the bearing capacity of soils reinforced by columns. Int. J. Numer. Anal. Methods Geomech. 29, 989–1004. http://dx.doi.org/10.1002/nag.441.

Karstunen, M., Krenn, H., Wheeler, S.J., Koskinen, M., Zentar, R., 2005. Effect of anisotropy and destructuration on the behavior of murro test embankment. Int. J. Geomech. 5, 87–97. http://dx.doi.org/10.1061/(asce)1532-3641(2005)5:2(87).

Koskinen, M., Karstunen, M., Wheeler, S.J., 2002. Modelling destructuration and anisotropy of a soft natural clay. In: Mestat (Ed.), Proceedings of the 5th European Conf. Numerical Methods in Geotechnical Engineering, Presses de l'ENPC/LCPS. Paris, pp. 11–20.

Lee, J.S., Pande, G.N., 1998. Analysis of stone-column reinforced foundations. Wiley Online Libr. 22, 1001–1020. http://dx.doi.org/10.1002/(SICI)1096-9853(199812)22:12<1001::AID-NAG955>3.0.CO;2-I.

Levasseur, S., Collin, F., Charlier, R., Kondo, D., 2011. Tunnel Excavation Modeling with Micromechanical Approaches. In: Springer Series in Geomechanics and Geoengineering, pp. 185–191. http://dx.doi.org/10.1007/978-94-007-1421-2_24.

Lorenzo, G.A., Bergado, D.T., 2006. Fundamental characteristics of cement-admixed clay in deep mixing. J. Mater. Civ. Eng. 18, 161–174. http://dx.doi.org/10.1061/(ASCE)0899-1561(2006)18:2(161).

Matsuoka, H., 1976. On the significance of the spatial mobilized plane. Soils Found. 16, 91–100.

Matsuoka, H., Nakai, T., 1974. Stress-deformation and strength characteristics of soil under three different principal stresses. In: Proceedings of the Japan Society of Civil Engineers. Japan Society of Civil Engineers, pp. 59–70.

Matsuoka, H., Nakai, T., 1982. A new failure criterion for soils in three dimensional stresses. In: IUTAM Conference on Deformation and Failure of Granular Materials. Delft, pp. 253–263.

Matsuoka, H., Nakai, T., 1985. Relationship among Tresca, Mises, Mohr–Coulomb and Matsuoka-Nakai failure criteria. Soils Found. 25, 123–128. http://dx.doi.org/10.3208/sandf1972.25.4_123.

Nakai, T., Matsuoka, H., 1983. Constitutive equation for soils based on the extended concept of spatial mobilized plane and its application to finite element analysis. Soils Found. 23, 87–105. http://dx.doi.org/10.3208/sandf1972.23.4_87.

Omine, K., Ochiai, H., Bolton, M., 2017. Homogenization method for numerical analysis of improved ground with cement-treated soil columns. In: Dry Mix Methods for Deep Soil Stabilization. Routledge, pp. 161–168.

Omine, K., Ochiai, H., Yoshida, N., 1998. Estimation of in-situ strength if cement-treated soils based on a two-phase mixture model. Soils Found. 38, 17–29. http://dx.doi.org/10.3208/sandf.38.4_17.

PLAXIS Scientific Model, 2023. PLAXIS 2D connect edition V23.02 - scientific manual manual. Bentley systems.

Reuss, A., 1929. Berechnung der fließgrenze von mischkristallen auf grund der plastizitätsbedingung für einkristalle. ZAMM - J. Appl. Math. Mech. / Z. Angew. Math. Mech. 9, 49–58. http://dx.doi.org/10.1002/zamm.19290090104.

Schanz, T., 1998. Zur modellierung des mechanischen verhaltens von reibungsmaterialen. Habilitation. In: Mitteilung 45 des Instituts für Geotechnik. (Ph.D. thesis). Universität Stuttgart.

Schanz, T., Vermeer, P.A., Bonnier, P.G., 1999. Beyond 2000 in Computational Geotechnics. Routledge, pp. 281–296. http://dx.doi.org/10.1201/9781315138206-27, chapter The hardening soil model: Formulation and verification.

Schweiger, H.F., Pande, G.N., 1988. Numerical analysis of a road embankment constructed in soft clay stabilised with stone columns.. In: Proceedings of the Sixth International Conference on Numerical Methods in Geomechanics. Innsbruck, pp. 1329–1333.

Sivasithamparam, N., Karstunen, M., Bonnier, P., 2015. Modelling creep behaviour of anisotropic soft soils. Comput. Geotech. 69, 46–57. http://dx.doi.org/10.1016/J.COMPGEO.2015.04.015.

Sivasithamparam, N., Karstunen, M., Brinkgreve, R.B., Bonnier, P.G., 2013. Comparison of two anisotropic creep models at element level. In: Installation Effects in Geotechnical Engineering - Proceedings of the International Conference on Installation Effects in Geotechnical Engineering. ICIEGE 2013, pp. 72–78. http://dx.doi.org/10.1201/b13890-12.

Sloan, S.W., 1987. Substepping schemes for the numerical integration of elastoplastic stress–strain relations. Internat. J. Numer. Methods Engrg. 24, 893–911. http://dx.doi.org/10.1002/nme.1620240505.

Tornborg, J., Karlsson, M., Kullingsjö, A., Karstunen, M., 2021. Modelling the construction and long-term response of Göta Tunnel. Comput. Geotech. 134, 104027. http://dx.doi.org/10.1016/j.compgeo.2021.104027.

van der Sluis, O., Schreurs, P., Meijer, H., 1999. Effective properties of a viscoplastic constitutive model obtained by homogenisation. Mech. Mater. 31, 743–759. http://dx.doi.org/10.1016/S0167-6636(99)00028-9.

Vogler, U., 2009. Numerical Modelling of Deep Mixing with Volume Averaging Technique (Ph.D. thesis). Department of Civil Engineering, University of Strathclyde, Glasgow, Scotland.

Vogler, U., Karstunen, M., 2008. Application of volume averaging technique in numerical modelling of deep mixing. In: Geotechnics of Soft Soils: Focus on Ground Improvement. CRC Press, pp. 201–208.

Voigt, W., 1889. Ueber die beziehung zwischen den beiden elasticitätsconstanten isotroper körper. Ann. Phys. 274, 573–587.

Wheeler, S.J., Näätänen, A., Karstunen, M., Lojander, M., 2003. An anisotropic elastoplastic model for soft clays. Can. Geotech. J. 40, 403–418. http://dx.doi.org/10.1139/t02-119.

Wiltafsky, C., 2003. S-Clay1s, User Defined Soil Model Documentation. Technical Report, University of Glasgow, Scotland.

Zdravkovic, L., Potts, D.M., St John, H.D., 2005. Modelling of a 3D excavation in finite element analysis. Géotechnique 55, 497–513. http://dx.doi.org/10.1680/geot.2005.55.7.497.